1 **Title**

2 **A Protein Kinase A-Regulated Network Encodes Short- and Long-Lived Cellular**

3 **Memory**

4

5

6

7 **Author names and affiliations**

8 Yanfei Jiang[1, §], Zohreh AkhavanAghdam[1, §], Yutian Li[1, §], Brian M. Zid[2], and Nan Hao[1,3*]

9

10 [1]Section of Molecular Biology, Division of Biological Sciences, University of California San Diego,

11 9500 Gilman Drive, La Jolla, CA 92093, USA

12 [2]Department of Chemistry and Biochemistry, University of California San Diego, 9500 Gilman Drive,

13 La Jolla, CA 92093, USA

14 [3]Lead Contact

15

16 [§]These authors contributed equally to this work.

17

18 **Contact**

19 *Correspondence: nhao@ucsd.edu

20

21

Abstract

Cells can store memories of prior experiences to modulate their responses to subsequent stresses, as seen for the protein kinase A (PKA)-mediated general stress response in yeast, which is required for resistance against future stressful conditions. Using microfluidics and time-lapse microscopy, we quantitatively analyzed how cellular memory of stress adaptation is encoded in single yeast cells. We found that cellular memory is biphasic. Short-lived memory was mediated by trehalose synthase and trehalose metabolism. Long-lived memory was mediated by PKA-regulated stress-responsive transcription factors and cytoplasmic messenger ribonucleoprotein (mRNP) granules. Strikingly, short- and long-lived memory could be selectively induced by different priming input dynamics. Computational modeling revealed how the PKA-mediated regulatory network could encode previous stimuli into memories with distinct dynamics. This biphasic memory-encoding scheme, analogous to innate and adaptive immune responses in mammals, might represent a general strategy to prepare for future challenges in rapidly changing environments.

Key words: systems biology, cellular memory, PKA, metabolism, mRNP granules**,** microfluidics, computational modeling, regulatory network, signaling dynamics

Introduction

Cells survive rapidly changing environments through adaptation mediated by sophisticated signaling and gene regulatory networks. How these networks operate dynamically to process complex extracellular signals and elicit appropriate responses remains a challenging question (Behar and Hoffmann, 2010; Levine et al., 2013; Purvis and Lahav, 2013). Recent advances in microfluidics and single-cell imaging technologies allow us to track the responses of individual living cells in a precisely controlled changing environment, providing a unique opportunity to elucidate the underlying principles for dynamic signal processing in cells (Bennett and Hasty, 2009). In this study, we exploited these cutting-edge technologies to systematically probe the regulatory network that enables cells to encode memory of prior environmental cues in order to modulate their adaptive responses to future challenges.

History-dependent cellular behaviors have been found in many organisms (Durrant and Dong, 2004; Hilker et al., 2016; Lou and Yousef, 1997; Matsumoto et al., 2007; Netea et al., 2015; Schenk et al., 2000; Scholz et al., 2005). For instance, it has been long established in the field of plant physiology that plant cells, once primed by mild stresses or chemical compounds, could obtain enhanced resistance to various future diseases and abiotic stresses (Prime et al., 2006; Savvides et al., 2016). In another oft-cited example, pre-treatment of human macrophages with interferon-γ significantly boosts subsequent lipopolysaccharide (LPS) responses against various pathogens and in tumor cell killing (Gifford and Lohmann-Matthes, 1987; Hayes et al., 1995). In this study, we referred these history-dependent responses in single cells as "cellular memory", which is of course fundamentally different from the neuronal memory in animals.

In the yeast *Saccharomyces cerevisiae*, a given stress can activate its specific response pathway as well as a common signaling pathway shared by a wide range of different stresses, called the general stress response (GSR) pathway (Gasch et al., 2000). This pathway is primarily mediated by protein

3

64   kinase A (PKA). In response to stresses, PKA is rapidly inhibited, leading to activation of downstream

65   transcription factors (TFs), such as Msn2 and Msn4, and the induction of hundreds of stress

66   responsive genes (Gorner et al., 1998; Hao and O'Shea, 2012; Jiang et al., 2017; Martinez-Pastor et

67   al., 1996). Previous studies have demonstrated that GSR is not required for survival against immediate

68   stress threats, but instead, is required for resistance against future stressful conditions (Berry and

69   Gasch, 2008; Berry et al., 2011; Guan et al., 2012). However, the mechanisms that mediate memory

70   encoding of environmental changes remain unclear.

71   In this study, we used GSR as a model to quantitatively analyze how PKA-dependent

72   regulatory processes operate dynamically to encode the memory of environmental changes. We

73   combined microfluidics with time-lapse microscopy to precisely control the dynamics of priming

74   inputs and to quantify the memory effect on stress adaptation in single cells. We found that cellular

75   memory shows two phases, a fast-decaying phase mediated by trehalose metabolism and a long-lasting

76   phase mediated by stress-activated TFs and messenger ribonucleoprotein (mRNP) granules.

77   Moreover, the memory dynamics can be modulated by priming inputs. Whereas a high amplitude

78   transient input specifically induces the fast-decaying phase of memory, a prolonged input is needed

79   to elicit the long-lasting memory effect. We further developed a computational model based on the

80   molecular processes identified experimentally. Our model quantitatively revealed the regulatory

81   scheme that encodes the information of previous environmental inputs into distinct memory

82   dynamics, implying a general strategy to optimize resource allocation and prepare for future challenges

83   under rapidly changing environments.

84

Results

PKA encodes biphasic cellular memory

Probing the effect of cellular memory has long been challenging, in part due to the difficulty in generating well-controlled sequential environmental changes in cell cultures. Recent advances in microfluidic technologies allow the precise control of extracellular conditions and tracking of the responses of single cells over extended periods (Hansen et al., 2015; Li et al., 2017a), providing a powerful tool for analyzing the memory behaviors in stress responses. In this study, we modified the channel design of an existing microfluidic device (Hao and O'Shea, 2012) to include separate control of three media inlets, one for the priming input, one for the normal growth medium, and one for the stress treatment (Fig. 1A). To increase the experimental throughput, we further aligned four individual channels into a single device to enable simultaneous running of multiple experiments, each with its own cell population and stimulus condition. Using this device, we first exposed the cells to a pulse of priming input followed by a "break time" with the normal growth medium. We then treated these primed cells with a sustained environmental stress and evaluated their adaptation responses. The device was mounted on a time-lapse microscope to track the responses of a large number of single cells throughout the entire experiment.

For the priming input, we used a chemical genetics strategy in which we introduced analog-sensitive mutations into the PKA isoforms so that they remain fully functional but can be specifically inhibited by the small molecular inhibitor, 1-NM-PP1 (Bishop et al., 2000). We have previously employed this strategy to control PKA activity, mimicking an upstream signaling event that specifically activates GSR, but not other stress specific pathways (AkhavanAghdam et al., 2016; Hansen and O'Shea, 2013; Hao et al., 2013; Hao and O'Shea, 2012) (Fig. 1B). Moreover, combined with time-lapse microscopy and microfluidics, it enables us to generate precisely controlled temporal

5

108   patterns of PKA inhibition as priming inputs and evaluate their effects on cells' adaptation to the

109   subsequent environmental stress.

110   For the subsequent stress treatment, we chose hyperosmotic stress (0.75M KCl) because the

111   stress adaptation process in individual cells can be reliably quantified using a specific reporter, the

112   stress-activated protein kinase Hog1, which we tagged with YFP. In response to osmotic stress, Hog1

113   rapidly translocates to the nucleus to induce an increase in intracellular osmolyte; once the osmolyte

114   balance is restored and the cell recovers from the stress, Hog1 exits the nucleus (Brewster and Gustin,

115   2014). There is a strong correlation between the timing of Hog1 nuclear export and the restoration

116   of cell volume (reflecting the turgor pressure recovery and cellular adaptation) (Muzzey et al., 2009).

117   Thus, the duration of Hog1 nuclear localization serves as a proxy for the time needed for the cell to

118   recover from a stress treatment: a shorter duration represents a faster adaptation while a longer

119   duration represents a slower adaptation.

120   Using Hog1 nuclear localization as a reporter, we observed that a 45-min priming input with

121   3 μM PKA inhibitor (Fig. 1C) , which causes full PKA inhibition (Hao et al., 2013; Hao and O'Shea,

122   2012), dramatically shortened the time needed to recover from hyperosmotic stress. Furthermore, the

123   effect of this priming input decays with increasing break times (Fig. 1D). To quantify the effect of

124   priming input and the dynamics of its decay, we measured and compared the durations of Hog1

125   nuclear translocation with and without the priming input (T_{primed}, $T_{unprimed}$) for each break time. For

126   instance, the priming input with a 10-min break time decreased the adaptation time by 34.7% from

127   40   min   to   26   min   (Fig.   1E).   We   defined   this   percentage   decrease   in   recovery

128   time $\left(\frac{T_{unprimed} - T_{primed}}{T_{unprimed}}\right) \times 100\%$ as a quantitative measure of the "memory effect" and use it

129   throughout our report.

130

131   We then plotted the memory effect as a function of break time. Notably, we observed that the

132   decay of memory effect is biphasic: About half of the memory effect was lost rapidly within 30

133   minutes, whereas the remaining memory effect plateaued until 90 minutes and then declined slowly

134   (Fig. 1F; Fig. S1). These biphasic memory dynamics were in contrast with the scenario where the

135   memory is primarily mediated by the expression of stress-resistance genes (Berry and Gasch, 2008;

136   Guan et al., 2012), which would follow an exponential decay trajectory as gene products are degraded

137   during the break time. We termed the fast-decaying component "short-lived" memory and the longer-

138   lasting component "long-lived" memory. To test whether the memory effect shows two phases under

139   natural stress conditions, we used 0.5M KCl as the priming input and observed similar biphasic

140   memory dynamics (Fig. S2), confirming that the memory pattern we found is not specific to chemical

141   inhibition of PKA.

142

143   **Short- and long-lived memory can be selectively induced by different priming input**

144   **dynamics**

145   We next considered how changing the dynamics of priming inputs impacts cellular memory.

146   To examine the effect of input duration on cellular memory, we exposed cells to a 15-min priming

147   input with 3 μM 1-NM-PP1 (Fig. 2A). In contrast to the response upon a 45-min priming input with

148   the same amplitude, cells only exhibited the fast-decaying component of memory effect and the long-

149   lasting phase is completely abolished (Fig. 2B, compare the blue versus dark pink curves). When

150   cycloheximide was added to inhibit protein synthesis during the priming experiment, this short-lived

151   memory effect was not affected (Fig. 2C), suggesting that short-lived memory does not depend on

152   gene expression, but may instead be mediated by metabolites or post-translational protein

153   modifications.

7

154   To further evaluate the effect of input amplitude on cellular memory, we treated cells with a

155   45-min priming input with lower amplitude (0.75 μM 1-NM-PP1), which causes partial inhibition of

156   PKA (Hao et al., 2013; Hao and O'Shea, 2012)(Fig. 2D). Under this condition, the fast-decaying

157   memory component and the plateau phase (0 – 90 minutes) of long-lived memory were both

158   abolished (Fig. 2E, compare the orange versus dark pink curves). Instead, cells displayed a slow

159   exponential decay trajectory, as would be expected if the memory effect is primarily mediated by gene

160   expression. In accordance, CHX abolished this memory effect (Fig. 2F), confirming that it requires

161   gene expression.

162   Taken together, these results demonstrated that the short- and long-lived components of

163   cellular memory could be dissected by modulating the amplitude and duration of priming inputs and

164   might be mediated by different molecular processes. Short-lived memory might be mediated through

165   a fast translation-independent process, whereas an input duration-dependent slow gene expression

166   process mediates the long-lasting memory, which could be further stabilized by another input

167   amplitude-dependent mechanism. The three types of priming inputs used here are referred to as:

168   "high-amplitude prolonged" (3 μM 1-NM-PP1, 45 min); "high-amplitude transient" (3 μM, 15 min);

169   and "low-amplitude prolonged" (0.75 μM, 45 min).

170

171   **Short-lived memory is mediated by trehalose synthesis and metabolism**

172   To determine the molecular process that mediates short-lived memory, we systematically

173   deleted 5 known or putative PKA phosphorylation targets (Gph1, Ctt1, Nth1, Gcy1, and Tps1)

174   involved in metabolic or stress-response pathways (Hwang et al., 1989; Schepers et al., 2012; Trevisol

175   et al., 2014) and examined their roles in mediating memory effect. Among these PKA targets, we

176   identified the trehalose synthase Tps1 (De Virgilio et al., 1993; Reinders et al., 1997), deletion of which

177   abolished short-lived memory (Fig. 3A). Trehalose is a simple carbohydrate produced in many

8

178 organisms that acts as membrane protectant and protein stabilizer to enhance cell survival under

179 stressful conditions (Hounsa et al., 1998). Note that the *tps1Δ hxk2Δ* strain was used because *tps1Δ* is

180 unable to grow on glucose, but this growth is restored in a *tps1Δ hxk2Δ* double mutant (Hohmann et

181 al., 1993). The deletion of *HXK2* alone does not affect the memory effect (Fig. 3A). We further

182 confirmed that the intracellular trehalose level is rapidly increased in response to the PKA inhibition

183 input and that this increase is lost when Tps1 is deleted (Fig. 3B). Since trehalose has been shown to

184 play an important role in cellular protection against osmotic stress (Hounsa et al., 1998), the increased

185 level of trehalose by the priming input could temporarily enhance the acquired resistance to the

186 subsequent osmotic stress, accounting for the observed short-lived memory.

187   To validate the central role of trehalose in short-lived memory, we manipulated its degradation.

188 Nth1 is a trehalose degradation enzyme, the activity of which is also regulated by PKA-dependent

189 phosphorylation (Schepers et al., 2012; Souza et al., 2002). We observed that, whereas short-term

190 memory was abolished in the absence of Tps1, it became prolonged when *NTH1* is deleted (Fig. S3,

191 compare the blue versus grey blue curves), suggesting that the activation of Nth1 accounts for the

192 fast decay rate of the trehalose level. In other words, the duration of short-lived memory is encoded

193 by the activity of Nth1.

194   To test whether Tps1 and trehalose also contribute to long-lived memory, we examined the

195 memory dynamics in response to the high-amplitude prolonged input (3 µM 1-NM-PP1, 45 min). We

196 found that the absence of Tps1 completely abolished the fast-decaying component of memory, while

197 long-lived memory remained unchanged (Fig. 3C, compare the red versus dark pink curves),

198 indicating that trehalose synthesis and metabolism contribute exclusively to short-lived memory. In

199 summary, these results showed that short-lived memory is mediated by PKA-dependent regulation

200 of Tps1 and Nth1, which control trehalose synthesis and metabolism (Fig. 3D).

201

Long-lived memory is mediated by stress-activated TFs and mRNP granules

We next investigated the processes underlying long-lived memory, which is gene expression-dependent, as suggested above in Fig. 2F. To determine the TFs that induce this response, we systematically deleted 6 PKA-regulated stress-responsive TFs (Gis1, Sko1, Hot1, Yap1, and Msn2/4) (Charizanis et al., 1999; Gorner et al., 1998; Hinnebusch and Natarajan, 2002; Pascual-Ahuir et al., 2001; Proft et al., 2001; Roosen et al., 2005) and examined their roles in mediating memory effect. We found that, whereas the deletion of Msn2/4 completely abolished long-lived memory in response to the 45 minutes, 0.75 µM 1-NM-PP1 priming input (Fig. S4A), the mutant showed only a partial loss of memory in response to the 3 µM 1-NM-PP1 priming input (Fig. S4B), suggesting that another TF might play a compensatory role under this condition. As the deletion of Yap1 also dramatically diminished long-lived memory in response to the 0.75 µM 1-NM-PP1 priming input (Fig. S4A), we generated the *msn2Δ msn4Δ yap1Δ* triple mutant and observed a complete loss of long-lived memory in the triple mutant (Fig. S4B). These results identified Msn2/4 and Yap1 as primary TFs that mediate the transcriptional response generating long-lasting memory. Moreover, we observed that the short- and long-lived memories are both abolished in the triple mutant (Fig. 4A and B). This loss of short-lived memory in the triple mutant is consistent with previous studies (Hansen and O'Shea, 2013; Norbeck and Blomberg, 2000), which showed that the expression of *TPS1*, required for short-lived memory, is completely dependent on the TFs deleted in the triple mutant.

We then investigated the mechanism that stabilizes long-lived memory, underlying the plateau phase of memory that is maintained up to 90 minutes after the removal of priming inputs (Fig. 1F). Previous studies have revealed that, in response to stress or PKA inhibition, cells accumulate a number of stress-responsive gene mRNAs in cytoplasmic mRNP granules, called processing-bodies (PBs) and stress granules (SGs), which regulate mRNA translation, decay, and storage (Decker and Parker, 2012; Ramachandran et al., 2011; Wang et al., 2018; Zid and O'Shea, 2014). PKA regulates

10

226   the formation of these mRNP granules by phosphorylating a PB scaffolding protein, Pat1

227   (Ramachandran et al., 2011). To test whether mRNP granules contribute to the memory effect, we

228   deleted Pat1, which is essential for the formation of PBs (Buchan et al., 2008; Ramachandran et al.,

229   2011). We observed that the plateau phase of long-lived memory was abolished in the *pat1Δ* strain

230   and the memory effect exhibited a continuous decay (Fig. 4C, compare the red versus dark pink

231   curves), indicating that PBs are required for maintaining the plateau phase. PBs and SGs are discrete

232   but functionally interacting compartments. Some mRNAs in PBs can be stored in a translationally

233   silenced state during stress and then return to translation via SGs upon stress removal (Buchan et al.,

234   2008; Decker and Parker, 2012). To determine the role of SGs in memory, we examined memory

235   dynamics in the absence of the SG component Pub1 (Buchan et al., 2008). We observed that, similar

236   to *pat1Δ*, *pub1Δ* cells no longer exhibited the plateau phase of memory (Fig. 4D, compare the red

237   versus dark pink curves). We note that *pub1Δ* cells have similar growth rate to that of WT throughout

238   the experiments, indicating that the plateau phase observed in WT is not related to cell growth rate.

239   These results suggested that the plateau phase of long-lived memory is dependent on the PBs/SGs-

240   mediated mRNA storage pathway. Notably, *pat1Δ* and *pub1Δ* showed higher memory levels than

241   those of WT for shorter break times (Fig. 4C and D, 15 - 30 mins), in agreement with the role of

242   PBs/SGs in mRNA translational silencing in addition to storage.

243   Furthermore, to confirm the localization of the mRNAs of stress responsive genes to mRNP

244   granules, we used the MS2 coat protein (MS2-CP) fused to GFP (Bertrand et al., 1998; Haim-

245   Vilmovsky and Gerst, 2009) to visualize the mRNAs of two well-characterized PKA-regulated stress

246   responsive genes, *DCS2* and *SIP18* (AkhavanAghdam et al., 2016; Hansen and O'Shea, 2013) in living

247   cells. We observed that, in response to the 3 µM 1-NM-PP1 input, the mRNAs of *DCS2* and *SIP18*

248   formed foci that co-localized with PBs as indicated by the PB marker Dcp2-mCherry (Brengues et

249   al., 2005) as well as some distinct granules (Fig. 4E). We have previously observed a similar localization

11

250   pattern for Msn2/4 targets, such as *GLC3* and *HXK1*, during glucose starvation (Zid and O'Shea,

251   2014). This localization pattern coincided with poor protein production from these mRNAs during

252   stress, suggesting that these stress-induced mRNAs are translationally silenced and stored in mRNP

253   granules to confer long-lasting cellular memory.

254   Taken together, these findings uncovered that two processes, gene transcription and mRNA

255   storage by mRNP granules, operate together to generate long-lived memory (Fig. 4F).

256

257   **Computational modeling suggested the network-mediated encoding of memory**

258   **dynamics**

259   From the experimental analysis described above, we delineated the regulatory processes that

260   mediate cellular memory. To quantitatively understand the dynamic encoding of memory, we

261   constructed a computational model. In the model, the network is composed of two memory-encoding

262   motifs, one for short-lived memory and the other for long-lived memory (Fig. 4F). The short-lived

263   memory motif comprises a fast process, in which PKA regulates the activities of Tps1 and Nth1 by

264   phosphorylation (Schepers et al., 2012; Trevisol et al., 2014). In response to PKA inhibition, Tps1 is

265   activated, boosting trehalose production; at the same time, Nth1 is inhibited, slowing down trehalose

266   degradation. As a result, the trehalose level increases rapidly. Subsequently, when the PKA inhibition

267   input is removed, Tps1 is inhibited while Nth1 is activated, leading to a rapid decline in trehalose

268   levels during the break time. This feedforward loop enables quick tuning of trehalose levels,

269   accounting for the fast-changing component of memory effect. The long-lived memory motif consists

270   of two processes that function together to regulate gene expression dynamics, a transcriptional

271   response mediated by TFs Yap1 and Msn2/4 (Smith et al., 1998) and a mRNA storage process

272   mediated by Pat1 (Decker and Parker, 2012). A detailed description of the model is included in the

273   Supplemental Materials.

274   With computationally obtained best-fit parameters, our model reproduced all the experimental

275   data (Fig. S5). In particular, in our model, the high-amplitude transient input (Fig. 5A, left panel)

276   specifically induces the trehalose production process (Fig. 5A, middle panel), generating the fast-

277   decaying memory (Fig. 5A, right panel, compare with data in Fig. 2B). The low-amplitude prolonged

278   input (Fig. 5B, left panel) only induce the transcriptional response but not the mRNP granule

279   formation, because the input is too weak, (Fig. 5B, middle panel), resulting in a slow exponential

280   decay of the memory effect after input removal (Fig. 5C, right panel, compare with data in Fig. 2E).

281   The high-amplitude prolonged input (Fig. 5C, left panel), however, leads to co-activation of the fast

282   trehalose production and the slow transcriptional response with mRNA storage by mRNP granules

283   (Fig. 5C, middle panel). Once the transcriptional response is initiated, a portion of the newly

284   synthesized stress resistance gene mRNAs is stored in mRNP granules via PKA regulation of Pat1.

285   Upon input removal, these mRNAs are slowly released and translated, resulting in a long-lasting (up

286   to ~90 minutes) memory plateau (Fig. 5C, right panel, compare with data in Fig. 1F). Consistent with

287   the model, we observed that only the high-amplitude prolonged input strongly induced the formation

288   of mRNP granules, as indicated by *DCS2* mRNA foci, whereas the high-amplitude transient input or

289   low-amplitude prolonged input could not (Fig. 5, right panel insets). These live-cell mRNA results

290   support our model in which the formation and function of mRNP granules depend on both the input

291   amplitude and duration. In summary, our model suggested that the three PKA-regulated processes,

292   trehalose metabolism, gene transcription and mRNP granule formation, operate and coordinate in a

293   temporal order to enable the biphasic memory dynamics observed experimentally.

294   Moreover, our model could nicely reproduce the memory dynamics observed in the mutants

295   of key regulatory factors. In the absence of Tps1, the priming input cannot induce the production of

296   trehalose (Fig. S6A, middle panel), resulting in a loss of the fast decaying component of memory,

297   while the long-lived memory remains intact (Fig. S6A, right panel, compare with data in Fig. 3C).

13

298   When the TFs Msn2/4 and Yap1 are deleted, the priming input can no longer induce the expression

299   of stress resistance genes, resulting in a loss of long-lived memory. Meanwhile, the absence of these

300   TFs leads to the loss of Tps1 expression that is required for the short-lived memory (Fig. S6B, middle

301   panel). As a result, both short- and long-lived memories are completely abolished (Fig. S6B, right

302   panel, compare with data in Fig. 4A). When Pat1 is deleted, the newly synthesized mRNAs, induced

303   by the priming input, can no longer be stored in mRNP granules (Fig. S6C, middle panel), but instead

304   they undergo immediate translation, resulting in a higher initial level of stress resistance than that of

305   WT (during break time $0 - 30$ min). This stress resistance, however, decays more quickly, as the gene

306   products are being directly and continuously degraded, and cells can no longer maintain a plateau of

307   long-lived memory (Fig. S6C, right panel, compare with data in Fig. 4C).

308

309   **Model prediction and experimental validation**

310   To further test our model, we used it to predict the memory dynamics in response to a

311   combined pattern of priming input. Neither low-amplitude prolonged input nor high-amplitude

312   transient input can induce the plateau phase of memory (Fig. 2B and E), yet our model predicted that

313   these two inputs, when applied sequentially (Fig. 6A), should be capable of generating a memory

314   plateau phase that is Pat1 dependent (Fig. 6B, "Prediction"). In this scenario, the low-amplitude

315   prolonged input would first produce a high level of mRNAs, and then the subsequent high-amplitude

316   transient input would induce mRNP granules to store newly synthesized mRNAs, enabling the plateau

317   phase. This prediction is intriguing because it illustrates that the memory effect to the combined input

318   is not simply the sum of the effects to the two single inputs (Fig. 6B, "Prediction", compare the purple

319   versus light pink curves) and this is attributed to the mRNP-dependent storage mechanism. Therefore,

320   since the memory-encoding processes are largely independent, when the mRNA storage process is

321   removed in the *pat1Δ* mutant, the memory effects would become additive (Fig. 6C, "Prediction"). We

14

322   experimentally tested these predictions, and, in agreement with the model, we observed a plateau

323   phase of memory in response to the combined input (Fig. 6B, "Experiment"). Moreover, in the

324   absence of Pat1, the plateau phase was abolished and the memory dynamics largely resembled the

325   sum of memory effects to the two single inputs (Fig. 6C, "Experiment"), consistent with the model

326   prediction.

327   These results validated our model and demonstrated its predictive power. Given that the

328   memory-encoding processes are kinetically separated, the model-guided analysis open a powerful

329   possibility to rationally design patterns of priming input and reprogram the temporal order of

330   regulatory processes for generating desired forms of memory dynamics.

15

Discussion

Cellular memory allows cells to adjust their responses to environmental cues based on their prior experience. In this study, we used GSR in yeast *Saccharomyces cerevisiae* as a model system and demonstrated that the memory effect on stress adaptation is biphasic, comprised of a fast decaying component (short-lived memory), mediated by post-translational regulation of the trehalose metabolism pathway, and a long-lasting component (long-lived memory), mediated by TFs and mRNP granules. These memory-encoding processes are mediated by PKA, a deeply conserved kinase with a central role in many molecular and cellular processes that is also associated with diverse diseases (Chiaradonna et al., 2008; Skalhegg and Tasken, 2000). Due to the functional pleiotropy of PKA, it has been difficult to target pharmacologically to achieve therapeutic specificity. Here we found that different PKA signaling dynamics, depending on the input amplitude and duration, could selectively induce specific downstream pathways or processes, leading to distinct memory dynamics. These results raise the possibility of perturbing the dynamics of signaling hubs for specific therapeutic outcomes (Behar et al., 2013; Li et al., 2017b).

Among the PKA-controlled processes, we want to emphasize the functional role of mRNP granules in maintaining cellular memory, which we revealed in this study. Cytoplasmic mRNP granules, such as PBs and SGs, play important roles in controlling the translation, degradation and storage of mRNAs upon environmental changes (Decker and Parker, 2012). Previous efforts have been focused on elucidating the biochemical and biophysical characteristics of mRNP granules (Mitchell and Parker, 2014). However, their functional roles in cell physiology remain largely unclear. Recent studies have begun to relate mRNP granules with cellular memory formation (Caudron and Barral, 2013; Chakrabortee et al., 2016; Dine et al., 2018; Standart and Weil, 2018). Our findings here provide independent strong evidence that the PKA-regulated mRNP granules contribute to a long-lasting memory of previous environmental challenges and facilitate the adaptation to future stresses.

16

355 Further analyses will systematically determine the identities of these stored mRNAs that mediate the

356 memory effect, the detailed mechanisms that direct these mRNAs to mRNP granules, and the

357 prevalence of this mRNP-dependent memory effect in regulating other cellular responses, such as the

358 hormetic effect on aging (Mattson, 2008).

359 In addition, through our modeling analysis, we obtained a quantitative understanding about

360 the dynamics of cellular memory and the regulatory network that controls these dynamics, both of

361 which remained largely missing from previous studies. The classic memory-generating networks

362 feature positive feedback loops that give rise to bistability, underlying the mechanisms for irreversible

363 processes such as cell-type differentiation (Chang et al., 2010; Wang et al., 2009; Xiong and Ferrell,

364 2003). In contrast, the network we identified is comprised of multiple parallel pathways with highly

365 diversified inherent kinetics. This network architecture confers signal processing capability and

366 plasticity in shaping memory dynamics, enabling cells to determine their memory patterns in response

367 to rapidly changing environments. In particular, this system couples two low-pass filters with different

368 thresholds to effectively separate the short-term responses to transient signals from the chronic ones

369 to prolonged signals. Moreover, the system also features a PKA-regulated mRNP granule formation

370 process, which represents a new network motif for biological information storage. The initiation of

371 the storage depends on the input amplitude, whereas how long the storage can last depends on the

372 amount of newly synthesized mRNAs being localized in the granules and hence depends on both the

373 amplitude and the duration of priming inputs. In this way, mRNP granules enable cells to integrate

374 the information about input amplitude and duration and tune the dynamics of their memory. Guided

375 by the dynamic regulatory schemes revealed by modeling, we further designed priming input patterns

376 to reprogram the temporal order of fast- and slow-acting processes in the network and reshape the

377 memory dynamics. For future studies, advanced fluorescent reporters and imaging technologies

378 (Aizer et al., 2014; Standart and Weil, 2018) could be employed to track the explicit spatiotemporal

17

379 dynamics of key species in the model, such as mRNAs and mRNP granules, in single cells. These

380 would enable us to constrain and improve our model and, ultimately, enhance the predictive power

381 of the model. We anticipate that a quantitative and predictive understanding of memory control

382 represents opportunities for broader and more effective use of priming treatments as a low-cost non-

383 genetic approach for stress management in agriculture, biotechnology, and clinical intervention.

384 Finally, we want to highlight the biological relevance of our findings. We revealed that, because

385 the molecular processes governing the two memory components have distinct kinetic properties,

386 short- and long-lived memories could be selectively induced by different dynamics of priming inputs.

387 Whereas a high amplitude transient input induces fast decaying memory that enables short-term stress

388 resistance, a prolonged input elicits long-lasting memory conferring long-term stress resistance. This

389 regulatory scheme is analogous to the fast responding innate immune response and the long-lasting

390 adaptive immune response in mammals. Moreover, the mRNP granules are responsive to the

391 amplitude and duration of inputs and can function as a knob to further tune the duration of the long-

392 term memory component based on the input dynamics. Taken together, this integrated regulatory

393 network enables cells to process the information of a previous stress encounter and determine how

394 long they need to keep the memory about it. We speculate that this type of regulation may represent

395 a strategy for cells to optimize resource allocation for future challenge preparation and may be widely

396 applicable to organisms living in rapidly changing environments. Furthermore, given that this

397 regulation is readily tunable, cells would be able to evolve their memory dynamics through natural

398 selection to match the environmental fluctuations in their habitats.

399

18

Acknowledgements

Author Contributions

Conceptualization, Y.J., Z.A., Y.L., B.Z., and N.H.; Methodology, Y.J., Z.A., Y.L., B.Z., and N.H.; Investigation, Y.J., Z.A., Y.L.; Formal Analysis, Y.J., Z.A., Y.L.; Writing - Original Draft, Y.J., Z.A., Y.L., and N.H.; Writing - Review & Editing, Y.J., Z.A., Y.L., B.Z., and N.H.; Resources, N.H.; Supervision, N.H.; Funding Acquisition, N.H.

Declaration of Interests

The authors declare no competing interests.

Materials and Methods

Strain Construction

Standard methods for the growth, maintenance, and transformation of yeast and bacteria and for manipulation of DNA were used throughout. All *Saccharomyces cerevisiae* strains used in this study are derived from the W303 background (*MATa leu2-3,112 trp1-1 can1-100 ura3-1 ade2-1 his3-11,15 GAL+ psi+ ADE+*). The strains used in this study are listed in Table 1.

Microfluidics

The previously reported Y-shape microfluidic device (AkhavanAghdam et al., 2016; Hao and O'Shea, 2012) with two inlets has been modified to accommodate three inlets on a single device and used in this study. The device fabrication and the setup of microfluidic experiments were performed as described previously (AkhavanAghdam et al., 2016; Hansen et al., 2015; Hao et al., 2013; Hao and O'Shea, 2012; Jiang et al., 2017).

Time-lapse microscopy

All time-lapse microscopy experiments were performed using a Nikon Ti-E inverted fluorescence microscope with an Andor iXon X3 DU897 EMCCD camera and a Spectra X LED light source. A CFI Plan Apochromat Lambda DM 60X Oil Immersion Objective (NA 1.40 WD 0.13MM) was used for all experiments. Three positions were chosen for each microfluidics channel. For each position, phase contrast, YFP, mCherry, and iRFP images were taken sequentially every two minutes. When the acquisition of the image series started, cells loaded in the microfluidic device were maintained in synthetic complete medium (SC, 2% dextrose) for the first five minutes before the introduction of 1-NM-PP1. Media input was switched manually between SC medium, SC medium with 1-NM-PP1 and SC medium with KCl at the indicated time points. The exposure and intensity settings for each fluorescence channel were set the same as that used in our earlier work (AkhavanAghdam et al., 2016).

For the priming experiments, cells were inoculated from a YPD plate into 2 ml SC liquid media two days before the experiment. On the second day, saturated cells were diluted by 1:20,000 into fresh SC media and grown overnight to reach OD = 0.6. These exponentially growing cells were diluted by 1:2 and grown for another 2 hours before being loaded into the microfluidic devices.

Image analysis

The images were processed using a custom MATLAB code for single-cell tracking and fluorescence quantification. The whole cell was segmented using the phase contrast images while the nucleus was segmented using the iRFP images. The cytoplasm was obtained by taking the difference of the whole cell and the nucleus. The nuclear to cytoplasmic ratios of Hog1-YFP were calculated using the mean fluorescence intensities of Hog1-YFP in the nucleus and in the cytoplasm. The ratios were subtracted by baseline which is the ratio right before KCl was introduced (close to 1) and then plotted against the time. The duration of Hog1 translocation for each condition was quantified using the full width at half maximum (FWHM) and used to calculate the memory effect for each break time, as illustrated in Fig. S1. We determine the sample size of our single-cell data based on similar studies published previously (AkhavanAghdam et al., 2016; Hansen and O'Shea, 2013; Hao et al., 2013; Hao and O'Shea, 2012).

Trehalose assay

Trehalose level was measured using the trehalose assay kit (Megazyme). Using this assay, trehalose

20

459 was converted into gluconate-6-phosphate, generating NADPH in a two-step reaction; the NADPH
460 concentration can be determined by measuring the absorbance at 340 nm. To determine trehalose
461 concentrations, 13 mL of yeast culture at OD≈0.5 was harvested and put on ice for 5 minutes before
462 centrifuged for 5 min at 4 °C. Cells were then washed with 0.1 M phosphate buffer (pH 5.9) to remove
463 glucose in media. After the wash, cells were resuspended in 1 ml 0.25 M Na_2CO_3 solution and OD
464 was measured. Additional Na_2CO_3 solution was added to make the cell densities (OD) the same for
465 0 and 20 min samples. Samples (~1 mL) were boiled for 20 min to release intracellular trehalose.
466 After cooling, the samples were centrifuged at 12 000 g for 3 min to remove cell debris. Two aliquots
467 (300 μl) of supernatant were transferred to two new tubes with one tube for total glucose level and
468 the other one for pre-existing glucose level. The following regents were then added to the cell lysates
469 sequentially: 150 μl acetic acid (1 M), 650 μl distilled water, 100 μL imidazole buffer (2 M imidazole,
470 100 mM magnesium chloride and 0.02% w/v sodium azide; pH 7.0), 50 μL NADP 1 /ATP (12.5
471 mg/mL $NADP^+$ and 36.7 mg/mL ATP) and 10 μL suspension of HK/G-6-PDH (425 U/mL
472 hexokinase and 212 U/mL glucose-6-phosphate dehydrogenase), 10 μL trehalase (490 U/mL). The
473 mixtures were incubated at room temperature for 5 min for the reactions. Absorbance at 340 nm was
474 recorded to determine the trehalose concentration in solution first. To estimate the intracellular
475 concentration, we assumed that cell density at OD=1 is $1x10^7$ cells/ml and yeast cell volume is 42 fl.
476 Pre-existing glucose was determined in a control reaction without added trehalase.

Live-cell mRNA visualization
479 The MS2-CP strains for mRNA visualization were constructed as described previously (Zid and
480 O'Shea, 2014). The promoter and the coding region of genes of interest (e.g. *DCS2*) were amplified
481 by PCR and then inserted into a template vector, which contains 12x MS2 loop sequences in the
482 integration vector pRS305. The plasmid was linearized by EcoRV and integrated into W303
483 background yeast strain with PKA analog-sensitive mutations (NH084) at the *LEU2* locus. A plasmid
484 that constitutively expresses MS2 coat proteins fused with GFP driven by *MYO2* promoter (Zid and
485 O'Shea, 2014) was also integrated into the same strain at *HIS3* locus. To visualize the colocalization
486 of mRNAs and PBs, a pRS304 plasmid that expresses *DCP2*-mCherry under the native *DCP2*
487 promoter was integrated into the same strain at *TRP1* locus (NH0857).

489 To perform live-cell mRNA visualization, cells were cultured to OD 0.6 and then loaded into
490 microfluidic devices for time-lapse microscopy. For each position, phase contrast, mCherry, GFP and
491 iRFP images were taken sequentially every two minutes. When the image acquisition started, cells
492 were maintained in SD media for the first five minutes to obtain a baseline for each fluorescence
493 channel prior to the introduction of 3 μM 1-NM-PP1 treatment.

495 The exposure and intensity settings for each channel were set as follows: GFP 200 ms at 9% lamp
496 intensity, mCherry 1s at 10% lamp intensity, and iRFP 300 ms at 15% lamp intensity.

Computational Modeling
499 Our model focuses on the PKA-dependent memory-encoding network, comprised of the
500 experimentally-identified processes that regulate the levels of metabolites or proteins needed for
501 enhancing stress adaptation, including trehalose and stress resistance gene products. The input of the
502 model is the PKA inhibition signal (priming input). For the model output, we assume that the memory
503 effect linearly depends on the sum of the amounts of trehalose and stress resistance gene products in
504 most of the kinetic regimes, unless the substance concentrations reach extremely high levels. This
505 assumption leaves out the explicit inclusion of the downstream Hog1 pathway in our model and

506 simplifies our analysis. The network consists of three molecular processes, trehalose metabolism,
507 stress resistance gene transcription and mRNP granule formation, all of which are PKA regulated.
508
509 For trehalose metabolism, PKA regulates both trehalose production and degradation by
510 phosphorylating Tps1 and Nth1, respectively. More specifically, PKA-mediated phosphorylation
511 inhibits Tps1 activity and enhances Nth1 activity based on the previous reports. Because the
512 regulation is primarily through phosphorylation, we assume that it is a fast process. For stress
513 resistance gene expression, PKA regulates mRNA transcription through transcription factors and
514 regulates mRNA translation and degradation through mRNP granules. More specifically, the PKA
515 inhibition input activates transcription factors and mRNP granules. Once the mRNP granules are
516 activated, a portion of the newly synthesized mRNAs is stored in mRNP granules where their
517 translation and degradation are paused. Upon input removal, these mRNAs are slowly released,
518 resuming their translation and degradation. Because gene transcription is a multi-step process, we
519 assume that it is a relatively slow process; in contrast, because PKA regulates mRNP granules through
520 phosphorylation, we assume that it is a relatively fast process. It should be noted that the level of
521 Tps1 is also dependent on PKA-regulated gene expression, resulting in a connection between the
522 trehalose metabolism pathway and the gene expression process. Based on the experimental
523 observations, these three processes have different dependence on input amplitude and duration.
524 Trehalose metabolism and mRNP granules can only be activated in response to high-amplitude
525 inputs; by contrast, mRNA transcription can be induced by low-amplitude input but a prolonged
526 duration is needed.

527 Computational modeling and all the simulations were done using the MATLAB. The model contains
528 13 variables and 27 independent parameters. The function "lsqnonlin" was used for data fitting. The
529 data of three dynamic inputs and three mutants (*tps1Δ*, *pat1Δ*, *msn2/4Δ yap1Δ*) were used for data
530 fitting (Fig. S5). To highlight the role of mRNP granules, time points for long-lived memory plateau
531 (Fig. 1F) were weighted by 20-fold for data fitting. Fitting starting with completely random guesses
532 failed. Therefore, we first manually chose parameter values that can qualitatively capture the data and
533 then used these manually-chosen parameters as the initial guesses for computational fitting. In order
534 to overcome the local minimum, we also tested 10 random sets of initial guesses which are randomly
535 chosen within 8 fold (1/8 to 8) of our first set of guesses and compared the squared norm of the
536 residuals of the final fitting results and then selected the best-fit set of parameter values.
537
538 The initial conditions are provided in Table S1. Reactions and rate constants are provided in Table
539 S2.
540
541
542 **Model Equations:**
543
544 $$\frac{d[TF_a]}{dt} = k_{11} \cdot [TF_i] - \frac{k_{12} \cdot PKA^4}{KM_3{}^4 + PKA^4} \cdot [TF_a]$$
545
546 $$\frac{d[TFi]}{dt} = -k_{11} \cdot [TF_i] + \frac{k_{12} \cdot PKA^4}{KM_3{}^4 + PKA^4} \cdot [TF_a]$$
547
548 $$\frac{d[Tps1RNA]}{dt} = \frac{k_{14} \cdot [TF_a]^2}{KM_8^2 + [TF_a]^2} + k_{15} - k_{16} \cdot [Tps1_{RNA}]$$

22

549

550
$$\frac{d[Tps1protein]}{dt} = k_{17} \cdot [Tps1RNA] - k_{13} \cdot [Tps1protein]$$

551

552
$$\frac{d[Nth1_a]}{dt} = \frac{k_1 \cdot PKA \cdot [Nth1_i]}{KM_4 + [Nth1_i]} - \frac{k_2 \cdot [Nth1_a]}{KM_6 + [Nth1_a]}$$

553

554
$$\frac{d[Nth1i]}{dt} = \frac{-k_1 \cdot PKA \cdot [Nth1_i]}{KM_4 + [Nth1_i]} + \frac{k_2 \cdot [Nth1_a]}{KM_6 + [Nth1_a]}$$

555

556
$$\frac{d[Trehalose]}{dt} = \frac{k_{19} \cdot KM_7{}^4}{KM_7^4 + PKA^4} \cdot [Tre6P] \cdot [Tps1protein] - \frac{k_{18} \cdot [Nth1_a]^4}{KM_9{}^4 + [Nth1_a]^4} \cdot [Trehalose]$$

557

558
$$\frac{d[Tre6P]}{dt} = \frac{-k_{19} \cdot KM_7{}^4}{KM_7{}^4 + PKA^4} \cdot [Tre6P] \cdot [Tps1protein]$$

559

560
$$\frac{d[Pat1_a]}{dt}$$

561
$$= -k_4 \cdot [Pat1_a] + \frac{k_3 \cdot KM_1{}^4}{KM_1{}^4 + PKA^4} \cdot [Pat1_i] - (1 - PKA) \cdot k_6 \cdot [mRNAs] \cdot [Pat1_a]$$

562
$$+ \frac{k_5 \cdot [mRNPs]}{KM_2 + [mRNPs]}$$

563

564
$$\frac{d[Pat1_i]}{dt} = k_4 \cdot [Pat1_a] - \frac{k_3 \cdot KM_1{}^4}{KM_1{}^4 + PKA^4} \cdot [Pat1_i]$$

565

566
$$\frac{d[mRNPs]}{dt} = (1 - PKA) \cdot k_6 \cdot [mRNAs] \cdot [Pat1_a] - \frac{k_5 \cdot [mRNPs]}{KM_2 + [mRNPs]}$$

567

568
$$\frac{d[mRNAs]}{dt} = k_{10} \cdot [TF_a] - k_9 \cdot [mRNAs] - (1 - PKA) \cdot k_6 \cdot [mRNAs] \cdot [Pat1_a] + \frac{k_5 \cdot [mRNPs]}{KM_2 + [mRNPs]}$$

569

570
$$\frac{d[protein]}{dt} = k_8 \cdot [mRNAs] - k_7 \cdot [protein]$$

571

572
$$output = [Trehalose] + \frac{0.25 \cdot [protein]^2}{0.0625 + [protein]^2}$$

573
574
575
576
577
578
579
580
581

23

582 **Strains used in this study**

583

Strain	Source	identifier
W303 MATa leu2-3,112 trp1-1 can1-100 ura3-1 ade2-1 his3-11,15 GAL+ psi+ ADE+, TPK1-M164G, TPK2-M147G, TPK3-M165G, NHP6a-iRFP-kanMX, MSN2-mCherry-TRP1, HOG1-YFP-HIS3	this study	NH0441
W303 MATa leu2-3,112 trp1-1 can1-100 ura3-1 ade2-1 his3-11,15 GAL+ psi+ ADE+, TPK1-M164G, TPK2-M147G, TPK3-M165G, NHP6a-iRFP-kanMX, MSN2-mCherry-TRP1, HOG1-YFP-HIS3, gph1::cgURA3	this study	NH0562
W303 MATa leu2-3,112 trp1-1 can1-100 ura3-1 ade2-1 his3-11,15 GAL+ psi+ ADE+, TPK1-M164G, TPK2-M147G, TPK3-M165G, NHP6a-iRFP-kanMX, MSN2-mCherry-TRP1, HOG1-YFP-HIS3, nth1::cgURA3	this study	NH0565
W303 MATa leu2-3,112 trp1-1 can1-100 ura3-1 ade2-1 his3-11,15 GAL+ psi+ ADE+, TPK1-M164G, TPK2-M147G, TPK3-M165G, NHP6a-iRFP-kanMX, MSN2-mCherry-TRP1, HOG1-YFP-HIS3, ctt1::cgURA3	this study	NH0566
W303 MATa leu2-3,112 trp1-1 can1-100 ura3-1 ade2-1 his3-11,15 GAL+ psi+ ADE+, TPK1-M164G, TPK2-M147G, TPK3-M165G, NHP6a-iRFP-kanMX, MSN2-mCherry-TRP1, HOG1-YFP-HIS3, gcy1::cgURA3	this study	NH0574
W303 MATa leu2-3,112 trp1-1 can1-100 ura3-1 ade2-1 his3-11,15 GAL+ psi+ ADE+, TPK1-M164G, TPK2-M147G, TPK3-M165G, NHP6a-iRFP-kanMX, MSN2-mCherry-TRP1, HOG1-YFP-HIS3, hxk2::cgLEU2	this study	NH0581
W303 MATa leu2-3,112 trp1-1 can1-100 ura3-1 ade2-1 his3-11,15 GAL+ psi+ ADE+, TPK1-M164G, TPK2-M147G, TPK3-M165G, NHP6a-iRFP-kanMX, MSN2-mCherry-TRP1, HOG1-YFP-HIS3, hxk2::cgLEU2, tps1::cgURA3	this study	NH0584
W303 MATa leu2-3,112 trp1-1 can1-100 ura3-1 ade2-1 his3-11,15 GAL+ psi+ ADE+, TPK1-M164G, TPK2-M147G, TPK3-M165G, NHP6a-iRFP-kanMX, MSN2-mCherry-TRP1, HOG1-YFP-HIS3, yap1::cgURA3	this study	NH0629
W303 MATa leu2-3,112 trp1-1 can1-100 ura3-1 ade2-1 his3-11,15 GAL+ psi+ ADE+, TPK1-M164G, TPK2-M147G, TPK3-M165G, NHP6a-iRFP-kanMX, MSN2-mCherry-TRP1, HOG1-YFP-HIS3, gis1::cgURA3	this study	NH0630
W303 MATa leu2-3,112 trp1-1 can1-100 ura3-1 ade2-1 his3-11,15 GAL+ psi+ ADE+, TPK1-M164G, TPK2-M147G, TPK3-M165G, NHP6a-iRFP-kanMX, MSN2-mCherry-TRP1, HOG1-YFP-HIS3, sko1::cgURA3	this study	NH0631
W303 MATa leu2-3,112 trp1-1 can1-100 ura3-1 ade2-1 his3-11,15 GAL+ psi+ ADE+, TPK1-M164G, TPK2-M147G, TPK3-M165G, NHP6a-iRFP-kanMX, MSN2-mCherry-TRP1, HOG1-YFP-HIS, hot1:cgURA3	this study	NH0633

24

W303 MATa leu2-3,112 trp1-1 can1-100 ura3-1 ade2-1 his3-11,15 GAL+ psi+ ADE+, TPK1-M164G, TPK2-M147G, TPK3-M165G, NHP6a-iRFP-kanMX, HOG1-mCitrine(V163A)-HIS, msn4::cgTRP1, msn2::natMX, yap1::cgURA3	this study	NH0641
W303 MATa leu2-3,112 trp1-1 can1-100 ura3-1 ade2-1 his3-11,15 GAL+ psi+ ADE+, TPK1-M164G, TPK2-M147G, TPK3-M165G, NHP6a-iRFP-kanMX, MSN2-mCherry-TRP1, HOG1-YFP-HIS3, msn4::cgTRP1, msn2::natMX	this study	NH0442
W303 MATa leu2-3,112 trp1-1 can1-100 ura3-1 ade2-1 his3-11,15 GAL+ psi+ ADE+, TPK1-M164G, TPK2-M147G, TPK3-M165G, NHP6a-iRFP-kanMX, MSN2-mCherry-TRP1, HOG1-YFP-HIS3, pub1::cgURA3	this study	NH0688
W303 MATa leu2-3,112 trp1-1 can1-100 ura3-1 ade2-1 his3-11,15 GAL+ psi+ ADE+, TPK1-M164G, TPK2-M147G, TPK3-M165G, NHP6a-iRFP-kanMX, MSN2-mCherry-TRP1, HOG1-YFP-HIS3, pat1::cgURA3	this study	NH0689
W303 MATa leu2-3,112 trp1-1 can1-100 ura3-1 ade2-1 his3-11,15 GAL+ psi+ ADE+, TPK1-M164G, TPK2-M147G, TPK3-M165G, Nhp6a-iRFP:kanMX, MS2-CP-GFP-HIS3	this study	NH0812
W303 MATa leu2-3,112 trp1-1 can1-100 ura3-1 ade2-1 his3-11,15 GAL+ psi+ ADE+, TPK1-M164G, TPK2-M147G, TPK3-M165G, Nhp6a-iRFP:kanMX, MS2-CP-GFP-HIS3, DCS2-12xMS2-LEU2, DCP2-mCherry-TRP1	this study	NH0857
W303 MATa leu2-3,112 trp1-1 can1-100 ura3-1 ade2-1 his3-11,15 GAL+ psi+ ADE+, TPK1-M164G, TPK2-M147G, TPK3-M165G, Nhp6a-iRFP:kanMX, MS2-CP-GFP-HIS3, SIP18-12xMS2-LEU2, DCP2-mCherry-TRP1	this study	NH0858

584

585 **Table S1. Initial conditions of all species in the model.**

586

Species	Initial conditions	Notes
TF_a	0	Active transcription factors, i.e. Msn2/4 and Yap1
TF_i	1	Active transcription factors
Tps1 mRNA	0.1	
Tps1 protein	1	
$Nth1_a$	0.2	Active Nth1
$Nth1_i$	0	Inactive Nth1
Trehalose	0	
Tre6P	0.35	Trehalose precursor, i.e. trehalose-6-P
$Pat1_a$	0	Active Pat1
$Pat1_i$	0.9	Inactive Pat1
mRNPs	0	mRNPs that stores mRNAs and induced by PKA inhibition
mRNAs	0	Stress responsive mRNAs induced by PKA inhibition

25

protein	0	Stress responsive proteins induced by PKA inhibition

Table S2. Best-fit parameter values used in the model.

Names	Parameters	Values
PKA activity	PKA	no inhibitor: 1 3μM1-NM-PP1: 0 0.75μM1-NM-PP1: 0.25
Transcription factor activation rate	k_{11}	0.009 min^{-1}
Transcription factor deactivation rate	k_{12}	50 min^{-1}
Transcription factor deactivation equilibrium constant	KM_3	1.3
Basal level of Tps1 mRNA transcription	k_{15}	0.01 min^{-1}
Tps1 mRNA transcription rate	k_{14}	0.4 min^{-1}
Tps1 mRNA degradation rate	k_{16}	0.05 min^{-1}
Tps1 translation rate	k_{17}	0.005 min^{-1}
Tps1 degradation rate	k_{13}	0.005 min^{-1}
Tps1 activation equilibrium constant	KM_6	0.01
Tps1 mRNA transcription equilibrium constant	KM_7	0.04
Nth1 activation rate	k_1	0.51 min^{-1}
Nth1 deactivation rate	k_2	0.5 min^{-1}
Nth1 activation equilibrium constant	KM_4	0.00001
Nth1 deactivation equilibrium constant	KM_5	0.00001
Trehalose production rate	k_{19}	0.02 min^{-1}
Trehalose decay rate (rate converting to downstream products)	k_{18}	0.41 min^{-1}
Trehalose decay equilibrium constant	KM_8	0.2
Pat1 activation rate	k_3	5 min^{-1}
Pat1 deactivation rate	k_4	0.5 min^{-1}
Pat1 activation equilibrium constant	KM_1	0.01
mRNPs formation rate	k_6	5 min^{-1}
mRNPs disassembly rate	k_5	0.01 min^{-1}
mRNPs disassembly equilibrium constant	KM_2	0.01
mRNA transcription rate	k_{10}	0.16 min^{-1}
mRNA degradation rate	k_9	0.02 min^{-1}
Stress resistance protein translation rate	k_8	3.2 min^{-1}
Stress resistance protein degradation rate	k_7	4 min^{-1}

26

REFERENCES

Aizer, A., Kalo, A., Kafri, P., Shraga, A., Ben-Yishay, R., Jacob, A., Kinor, N., and Shav-Tal, Y. (2014). Quantifying mRNA targeting to P-bodies in living human cells reveals their dual role in mRNA decay and storage. J Cell Sci *127*, 4443-4456.

AkhavanAghdam, Z., Sinha, J., Tabbaa, O.P., and Hao, N. (2016). Dynamic control of gene regulatory logic by seemingly redundant transcription factors. Elife *5*.

Behar, M., Barken, D., Werner, S.L., and Hoffmann, A. (2013). The dynamics of signaling as a pharmacological target. Cell *155*, 448-461.

Behar, M., and Hoffmann, A. (2010). Understanding the temporal codes of intra-cellular signals. Curr Opin Genet Dev *20*, 684-693.

Bennett, M.R., and Hasty, J. (2009). Microfluidic devices for measuring gene network dynamics in single cells. Nat Rev Genet *10*, 628-638.

Berry, D.B., and Gasch, A.P. (2008). Stress-activated genomic expression changes serve a preparative role for impending stress in yeast. Mol Biol Cell *19*, 4580-4587.

Berry, D.B., Guan, Q., Hose, J., Haroon, S., Gebbia, M., Heisler, L.E., Nislow, C., Giaever, G., and Gasch, A.P. (2011). Multiple means to the same end: the genetic basis of acquired stress resistance in yeast. PLoS Genet *7*, e1002353.

Bertrand, E., Chartrand, P., Schaefer, M., Shenoy, S.M., Singer, R.H., and Long, R.M. (1998). Localization of ASH1 mRNA particles in living yeast. Mol Cell *2*, 437-445.

Bishop, A.C., Ubersax, J.A., Petsch, D.T., Matheos, D.P., Gray, N.S., Blethrow, J., Shimizu, E., Tsien, J.Z., Schultz, P.G., Rose, M.D.*, et al.* (2000). A chemical switch for inhibitor-sensitive alleles of any protein kinase. Nature *407*, 395-401.

Brengues, M., Teixeira, D., and Parker, R. (2005). Movement of eukaryotic mRNAs between polysomes and cytoplasmic processing bodies. Science *310*, 486-489.

Brewster, J.L., and Gustin, M.C. (2014). Hog1: 20 years of discovery and impact. Sci Signal *7*, re7.

Buchan, J.R., Muhlrad, D., and Parker, R. (2008). P bodies promote stress granule assembly in Saccharomyces cerevisiae. J Cell Biol *183*, 441-455.

Caudron, F., and Barral, Y. (2013). A super-assembly of Whi3 encodes memory of deceptive encounters by single cells during yeast courtship. Cell *155*, 1244-1257.

Chakrabortee, S., Byers, J.S., Jones, S., Garcia, D.M., Bhullar, B., Chang, A., She, R., Lee, L., Fremin, B., Lindquist, S.*, et al.* (2016). Intrinsically Disordered Proteins Drive Emergence and Inheritance of Biological Traits. Cell *167*, 369-381 e312.

Chang, D.E., Leung, S., Atkinson, M.R., Reifler, A., Forger, D., and Ninfa, A.J. (2010). Building biological memory by linking positive feedback loops. Proc Natl Acad Sci U S A *107*, 175-180.

Charizanis, C., Juhnke, H., Krems, B., and Entian, K.D. (1999). The oxidative stress response mediated via Pos9/Skn7 is negatively regulated by the Ras/PKA pathway in Saccharomyces cerevisiae. Mol Gen Genet *261*, 740-752.

Chiaradonna, F., Balestrieri, C., Gaglio, D., and Vanoni, M. (2008). RAS and PKA pathways in cancer: new insight from transcriptional analysis. Front Biosci *13*, 5257-5278.

De Virgilio, C., Burckert, N., Bell, W., Jeno, P., Boller, T., and Wiemken, A. (1993). Disruption of TPS2, the gene encoding the 100-kDa subunit of the trehalose-6-phosphate synthase/phosphatase complex in Saccharomyces cerevisiae, causes accumulation of trehalose-6-phosphate and loss of trehalose-6-phosphate phosphatase activity. Eur J Biochem *212*, 315-323.

Decker, C.J., and Parker, R. (2012). P-bodies and stress granules: possible roles in the control of translation and mRNA degradation. Cold Spring Harb Perspect Biol *4*, a012286.

Dine, E., Gil, A.A., Uribe, G., Brangwynne, C.P., and Toettcher, J.E. (2018). Protein Phase Separation Provides Long-Term Memory of Transient Spatial Stimuli. Cell Syst *6*, 655-663 e655.

Durrant, W.E., and Dong, X. (2004). Systemic acquired resistance. Annu Rev Phytopathol *42*, 185-209.

Gasch, A.P., Spellman, P.T., Kao, C.M., Carmel-Harel, O., Eisen, M.B., Storz, G., Botstein, D., and Brown, P.O. (2000). Genomic expression programs in the response of yeast cells to environmental changes. Mol Biol Cell *11*, 4241-4257.

Gifford, G.E., and Lohmann-Matthes, M.L. (1987). Gamma interferon priming of mouse and human macrophages for induction of tumor necrosis factor production by bacterial lipopolysaccharide. J Natl Cancer Inst *78*, 121-124.

Gorner, W., Durchschlag, E., Martinez-Pastor, M.T., Estruch, F., Ammerer, G., Hamilton, B., Ruis, H., and Schuller, C. (1998). Nuclear localization of the C2H2 zinc finger protein Msn2p is regulated by stress and protein kinase A activity. Genes Dev *12*, 586-597.

Guan, Q., Haroon, S., Bravo, D.G., Will, J.L., and Gasch, A.P. (2012). Cellular memory of acquired stress resistance in Saccharomyces cerevisiae. Genetics *192*, 495-505.

Haim-Vilmovsky, L., and Gerst, J.E. (2009). m-TAG: a PCR-based genomic integration method to visualize the localization of specific endogenous mRNAs in vivo in yeast. Nat Protoc *4*, 1274-1284.

Hansen, A.S., Hao, N., and O'Shea, E.K. (2015). High-throughput microfluidics to control and measure signaling dynamics in single yeast cells. Nat Protoc *10*, 1181-1197.

Hansen, A.S., and O'Shea, E.K. (2013). Promoter decoding of transcription factor dynamics involves a trade-off between noise and control of gene expression. Mol Syst Biol *9*, 704.

Hao, N., Budnik, B.A., Gunawardena, J., and O'Shea, E.K. (2013). Tunable signal processing through modular control of transcription factor translocation. Science *339*, 460-464.

Hao, N., and O'Shea, E.K. (2012). Signal-dependent dynamics of transcription factor translocation controls gene expression. Nat Struct Mol Biol *19*, 31-39.

Hayes, M.P., Freeman, S.L., and Donnelly, R.P. (1995). IFN-gamma priming of monocytes enhances LPS-induced TNF production by augmenting both transcription and MRNA stability. Cytokine *7*, 427-435.

Hilker, M., Schwachtje, J., Baier, M., Balazadeh, S., Baurle, I., Geiselhardt, S., Hincha, D.K., Kunze, R., Mueller-Roeber, B., Rillig, M.C.*, et al.* (2016). Priming and memory of stress responses in organisms lacking a nervous system. Biol Rev Camb Philos Soc *91*, 1118-1133.

Hinnebusch, A.G., and Natarajan, K. (2002). Gcn4p, a master regulator of gene expression, is controlled at multiple levels by diverse signals of starvation and stress. Eukaryot Cell *1*, 22-32.

Hohmann, S., Neves, M.J., de Koning, W., Alijo, R., Ramos, J., and Thevelein, J.M. (1993). The growth and signalling defects of the ggs1 (fdp1/byp1) deletion mutant on glucose are suppressed by a deletion of the gene encoding hexokinase PII. Curr Genet *23*, 281-289.

Hounsa, C.G., Brandt, E.V., Thevelein, J., Hohmann, S., and Prior, B.A. (1998). Role of trehalose in survival of Saccharomyces cerevisiae under osmotic stress. Microbiology *144 (Pt 3)*, 671-680.

Hwang, P.K., Tugendreich, S., and Fletterick, R.J. (1989). Molecular analysis of GPH1, the gene encoding glycogen phosphorylase in Saccharomyces cerevisiae. Mol Cell Biol *9*, 1659-1666.

Jiang, Y., AkhavanAghdam, Z., Tsimring, L.S., and Hao, N. (2017). Coupled feedback loops control the stimulus-dependent dynamics of the yeast transcription factor Msn2. J Biol Chem *292*, 12366-12372.

Levine, J.H., Lin, Y., and Elowitz, M.B. (2013). Functional roles of pulsing in genetic circuits. Science *342*, 1193-1200.

Li, Y., Jin, M., O'Laughlin, R., Bittihn, P., Tsimring, L.S., Pillus, L., Hasty, J., and Hao, N. (2017a). Multigenerational silencing dynamics control cell aging. Proc Natl Acad Sci U S A *114*, 11253-11258.

28

691 Li, Y., Roberts, J., AkhavanAghdam, Z., and Hao, N. (2017b). Mitogen-activated protein kinase
692 (MAPK) dynamics determine cell fate in the yeast mating response. J Biol Chem *292*, 20354-20361.
693 Lou, Y., and Yousef, A.E. (1997). Adaptation to sublethal environmental stresses protects Listeria
694 monocytogenes against lethal preservation factors. Appl Environ Microbiol *63*, 1252-1255.
695 Martinez-Pastor, M.T., Marchler, G., Schuller, C., Marchler-Bauer, A., Ruis, H., and Estruch, F. (1996).
696 The Saccharomyces cerevisiae zinc finger proteins Msn2p and Msn4p are required for transcriptional
697 induction through the stress response element (STRE). EMBO J *15*, 2227-2235.
698 Matsumoto, H., Hamada, N., Takahashi, A., Kobayashi, Y., and Ohnishi, T. (2007). Vanguards of
699 paradigm shift in radiation biology: radiation-induced adaptive and bystander responses. J Radiat Res
700 *48*, 97-106.
701 Mattson, M.P. (2008). Hormesis defined. Ageing Res Rev *7*, 1-7.
702 Mitchell, S.F., and Parker, R. (2014). Principles and properties of eukaryotic mRNPs. Mol Cell *54*,
703 547-558.
704 Muzzey, D., Gomez-Uribe, C.A., Mettetal, J.T., and van Oudenaarden, A. (2009). A systems-level
705 analysis of perfect adaptation in yeast osmoregulation. Cell *138*, 160-171.
706 Netea, M.G., Latz, E., Mills, K.H., and O'Neill, L.A. (2015). Innate immune memory: a paradigm
707 shift in understanding host defense. Nat Immunol *16*, 675-679.
708 Norbeck, J., and Blomberg, A. (2000). The level of cAMP-dependent protein kinase A activity
709 strongly affects osmotolerance and osmo-instigated gene expression changes in Saccharomyces
710 cerevisiae. Yeast *16*, 121-137.
711 Pascual-Ahuir, A., Posas, F., Serrano, R., and Proft, M. (2001). Multiple levels of control regulate the
712 yeast cAMP-response element-binding protein repressor Sko1p in response to stress. J Biol Chem
713 *276*, 37373-37378.
714 Prime, A.P.G., Conrath, U., Beckers, G.J., Flors, V., Garcia-Agustin, P., Jakab, G., Mauch, F.,
715 Newman, M.A., Pieterse, C.M., Poinssot, B.*, et al.* (2006). Priming: getting ready for battle. Mol Plant
716 Microbe Interact *19*, 1062-1071.
717 Proft, M., Pascual-Ahuir, A., de Nadal, E., Arino, J., Serrano, R., and Posas, F. (2001). Regulation of
718 the Sko1 transcriptional repressor by the Hog1 MAP kinase in response to osmotic stress. EMBO J
719 *20*, 1123-1133.
720 Purvis, J.E., and Lahav, G. (2013). Encoding and decoding cellular information through signaling
721 dynamics. Cell *152*, 945-956.
722 Ramachandran, V., Shah, K.H., and Herman, P.K. (2011). The cAMP-dependent protein kinase
723 signaling pathway is a key regulator of P body foci formation. Mol Cell *43*, 973-981.
724 Reinders, A., Burckert, N., Hohmann, S., Thevelein, J.M., Boller, T., Wiemken, A., and De Virgilio,
725 C. (1997). Structural analysis of the subunits of the trehalose-6-phosphate synthase/phosphatase
726 complex in Saccharomyces cerevisiae and their function during heat shock. Mol Microbiol *24*, 687-
727 695.
728 Roosen, J., Engelen, K., Marchal, K., Mathys, J., Griffioen, G., Cameroni, E., Thevelein, J.M., De
729 Virgilio, C., De Moor, B., and Winderickx, J. (2005). PKA and Sch9 control a molecular switch
730 important for the proper adaptation to nutrient availability. Mol Microbiol *55*, 862-880.
731 Savvides, A., Ali, S., Tester, M., and Fotopoulos, V. (2016). Chemical Priming of Plants Against
732 Multiple Abiotic Stresses: Mission Possible? Trends Plant Sci *21*, 329-340.
733 Schenk, P.M., Kazan, K., Wilson, I., Anderson, J.P., Richmond, T., Somerville, S.C., and Manners,
734 J.M. (2000). Coordinated plant defense responses in Arabidopsis revealed by microarray analysis. Proc
735 Natl Acad Sci U S A *97*, 11655-11660.

736 Schepers, W., Van Zeebroeck, G., Pinkse, M., Verhaert, P., and Thevelein, J.M. (2012). In vivo
737 phosphorylation of Ser21 and Ser83 during nutrient-induced activation of the yeast protein kinase A
738 (PKA) target trehalase. J Biol Chem *287*, 44130-44142.
739 Scholz, H., Franz, M., and Heberlein, U. (2005). The hangover gene defines a stress pathway required
740 for ethanol tolerance development. Nature *436*, 845-847.
741 Skalhegg, B.S., and Tasken, K. (2000). Specificity in the cAMP/PKA signaling pathway. Differential
742 expression,regulation, and subcellular localization of subunits of PKA. Front Biosci *5*, D678-693.
743 Smith, A., Ward, M.P., and Garrett, S. (1998). Yeast PKA represses Msn2p/Msn4p-dependent gene
744 expression to regulate growth, stress response and glycogen accumulation. EMBO J *17*, 3556-3564.
745 Souza, A.C., De Mesquita, J.F., Panek, A.D., Silva, J.T., and Paschoalin, V.M. (2002). Evidence for a
746 modulation of neutral trehalase activity by Ca2+ and cAMP signaling pathways in Saccharomyces
747 cerevisiae. Brazilian journal of medical and biological research = Revista brasileira de pesquisas
748 medicas e biologicas *35*, 11-16.
749 Standart, N., and Weil, D. (2018). P-Bodies: Cytosolic Droplets for Coordinated mRNA Storage.
750 Trends Genet *34*, 612-626.
751 Trevisol, E.T., Panek, A.D., De Mesquita, J.F., and Eleutherio, E.C. (2014). Regulation of the yeast
752 trehalose-synthase complex by cyclic AMP-dependent phosphorylation. Biochim Biophys Acta *1840*,
753 1646-1650.
754 Wang, C., Schmich, F., Srivatsa, S., Weidner, J., Beerenwinkel, N., and Spang, A. (2018). Context-
755 dependent deposition and regulation of mRNAs in P-bodies. Elife *7*.
756 Wang, L., Walker, B.L., Iannaccone, S., Bhatt, D., Kennedy, P.J., and Tse, W.T. (2009). Bistable
757 switches control memory and plasticity in cellular differentiation. Proc Natl Acad Sci U S A *106*,
758 6638-6643.
759 Xiong, W., and Ferrell, J.E., Jr. (2003). A positive-feedback-based bistable 'memory module' that
760 governs a cell fate decision. Nature *426*, 460-465.
761 Zid, B.M., and O'Shea, E.K. (2014). Promoter sequences direct cytoplasmic localization and
762 translation of mRNAs during starvation in yeast. Nature *514*, 117-121.
763
764
765
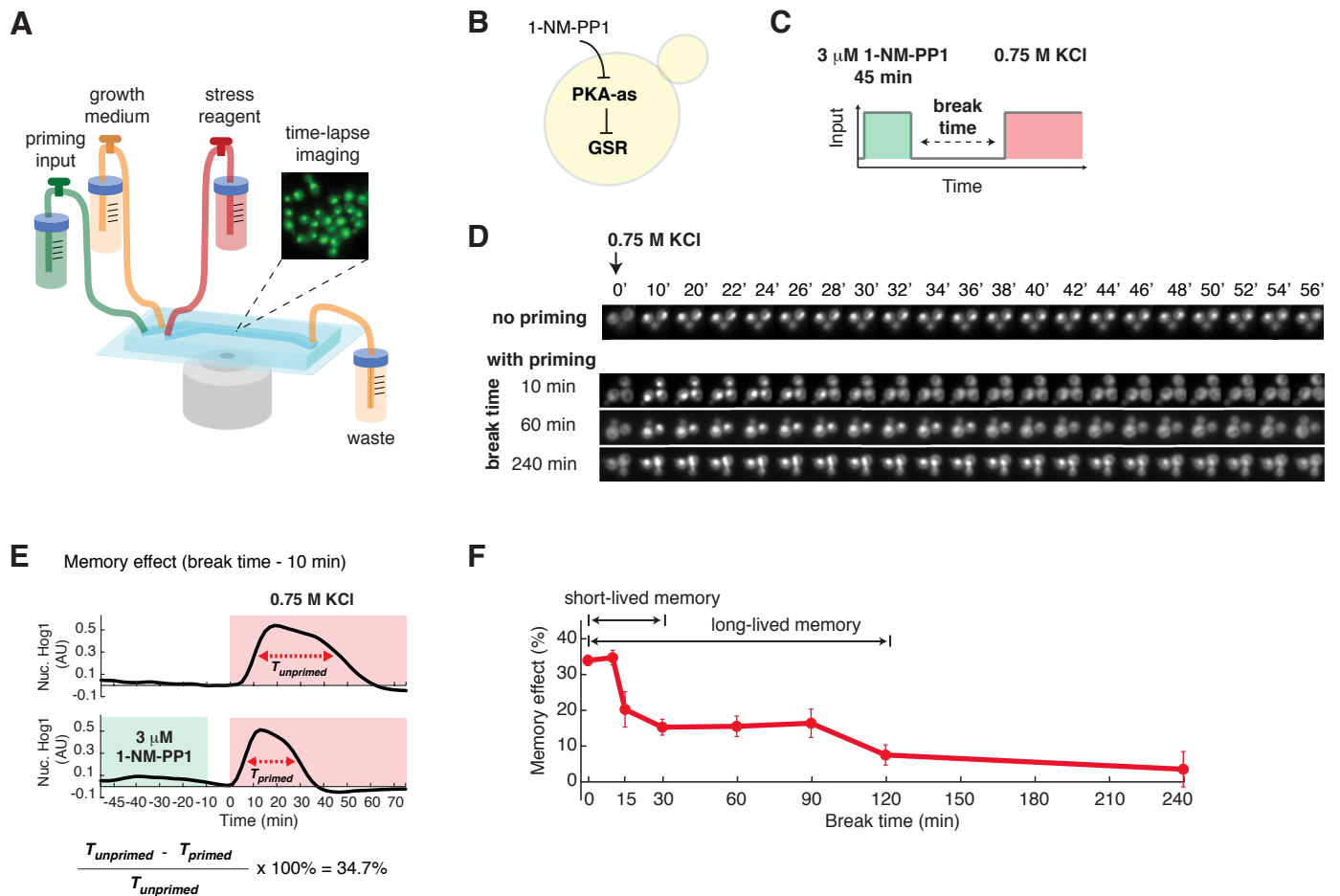
Figure 1. PKA encodes biphasic cellular memory. (A) A diagram of the microfluidic system used in priming experiments. The microfluidic device contains three inlets for priming input, growth medium, and stress reagent, respectively. Yeast cells were immobilized in the culturing chamber for time-lapse microscopic imaging. The medium flow from the inlets to the waste is driven by gravity. The three inlets can be opened/closed to allow medium switching during the experiment. (B) A diagram describes the analog sensitive PKA strain used in this study. (C) A schematic of the experimental design. Within the microfluidic device, cells were first exposed to a pulse of 1-NM-PP1 priming input, followed by a break time of normal growth medium. These primed cells were then exposed to sustained 0.75 M KCl treatment. (D) Representative time-lapse images of Hog1 nuclear translocation in the priming experiments with different break times. Left panel - schematic illustration of the priming experiments. (E) Time traces of Hog1 translocation in response to 0.75 M KCl (red shaded) without (top) or with (bottom) 45 min priming with 3 μM 1-NM-PP1 (green shaded) followed by 10 min break time. The duration of nuclear localization was quantified using the full width at half maximum (FWHM) in single cells (Tprimed and Tunprimed). The memory effect has been calculated using Tprimed and Tunprimed. (F) Biphasic memory dynamics in response to the high-amplitude prolonged priming input (panel C). The plot shows the relationship of memory effect versus break time. Data points are averages of at least three independent experiments. Error bars – standard error of the mean (SEM). The Hog1 time trace for each break time is shown in Figure S1.
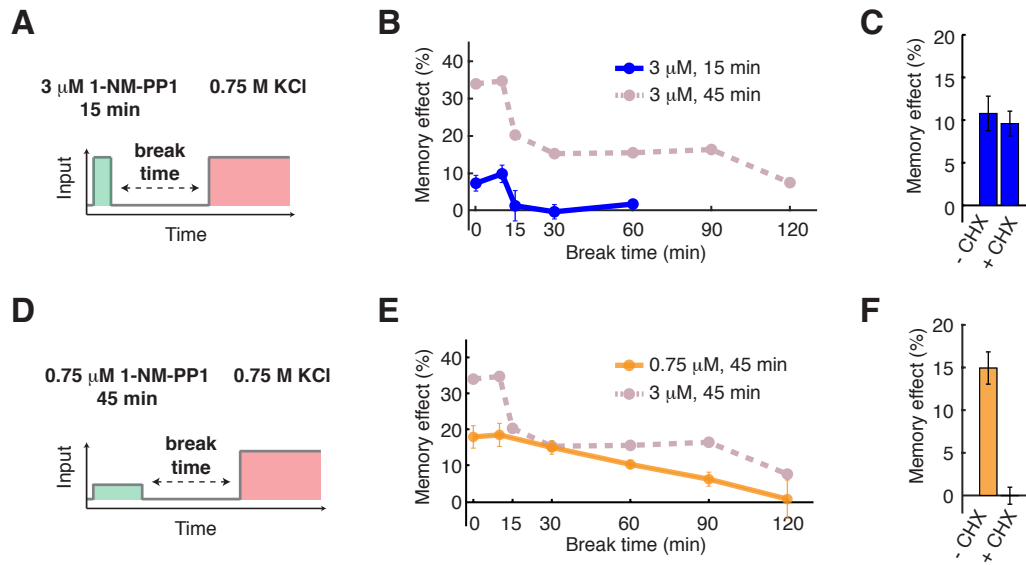
Figure 2. Short- and long-lived memory can be selectively induced by different priming input dynamics. (A) A schematic of the priming experiment with the high-amplitude transient priming input (15 min, 3 μM 1-NM-PP1). (B) The dynamics of memory effect in response to the high-amplitude transient priming input. Dashed line in dark pink represents the memory dynamics from Fig. 1F and is included in the plot for comparison. (C) The dependence of short-lived memory effect on translation. The bar graph shows the memory effects in response to 15 min, 3 μM 1-NM-PP1 priming input with a 10 min break time, with or without 10 μg/mL cycloheximide treatment (CHX). (D) A schematic of the priming experiment with the low-amplitude prolonged priming input (45 min, 0.75 μM 1-NM-PP1). (E) The dynamics of memory effect in response to the low-amplitude prolonged priming input. Dashed line in dark pink represents the memory dynamics from Fig. 1F and is included in the plot for comparison. (F) The dependence of long-lived memory effect on translation. The bar graph shows the memory effects in response to 45 min, 0.75 μM 1-NM-PP1 priming input with a 30 min break time, with or without the CHX treatment. Data points are averages of at least three independent experiments. Error bars – SEM.
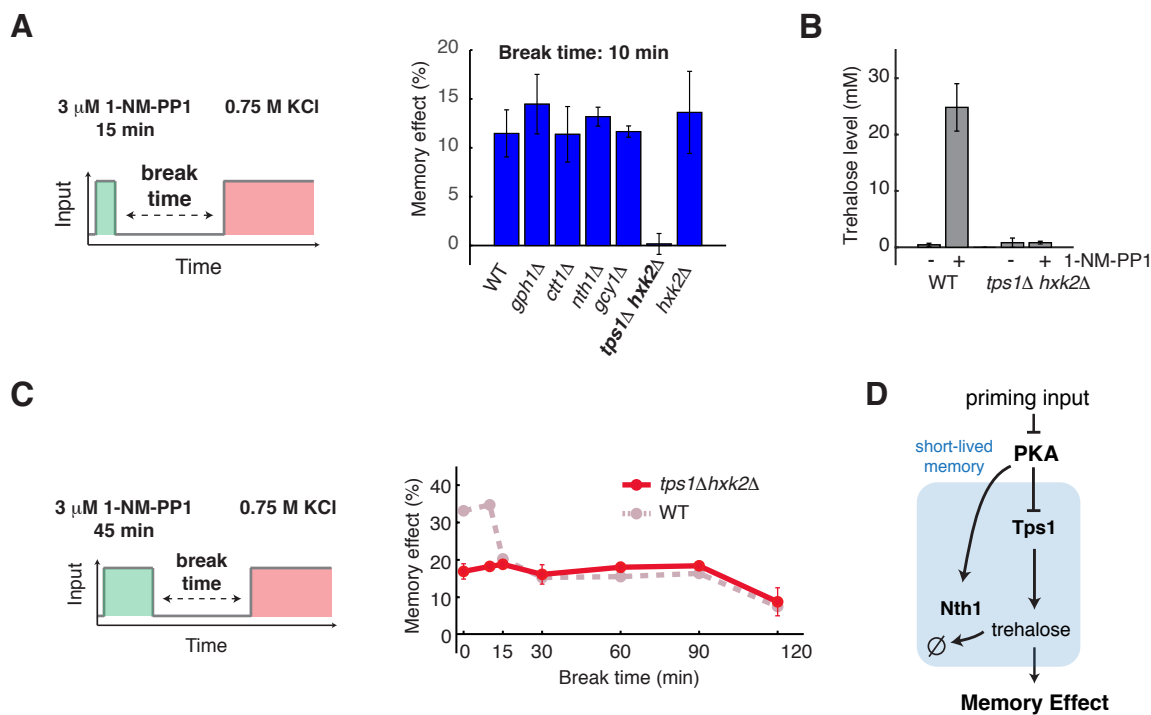
Figure 3. Short-lived memory is mediated by trehalose synthesis and metabolism. (A) Identification of Tps1 in mediating short-term memory. The bar graph shows the memory effects in response to the high-amplitude transient priming input (15 min, 3 μM 1-NM-PP1) with a 10 min break time in WT and mutant strains. (B) Intracellular trehalose level increases in response to PKA inhibition. Bar graph shows trehalose levels in WT and *tps1Δ hxk2Δ*, with and without PKA inhibition. Trehalose levels were measured after a 20-min treatment of 3 μM 1-NM-PP1. (C) Memory dynamics in *tps1Δ hxk2Δ* in response to the high-amplitude prolonged priming input (45 min, 3 μM 1-NM-PP1). Left panel, the schematic illustrating the treatment procedure of the priming experiment. Right panel, memory dynamics in *tps1Δ hxk2Δ*. Dashed lines in dark pink represent the memory dynamics in WT (from Fig. 1F) and are included in the plots for comparison. Data points are averages of at least three independent experiments. Error bars – SEM. (D) A diagram illustrates the network motif that gives rise to short-lived memory.
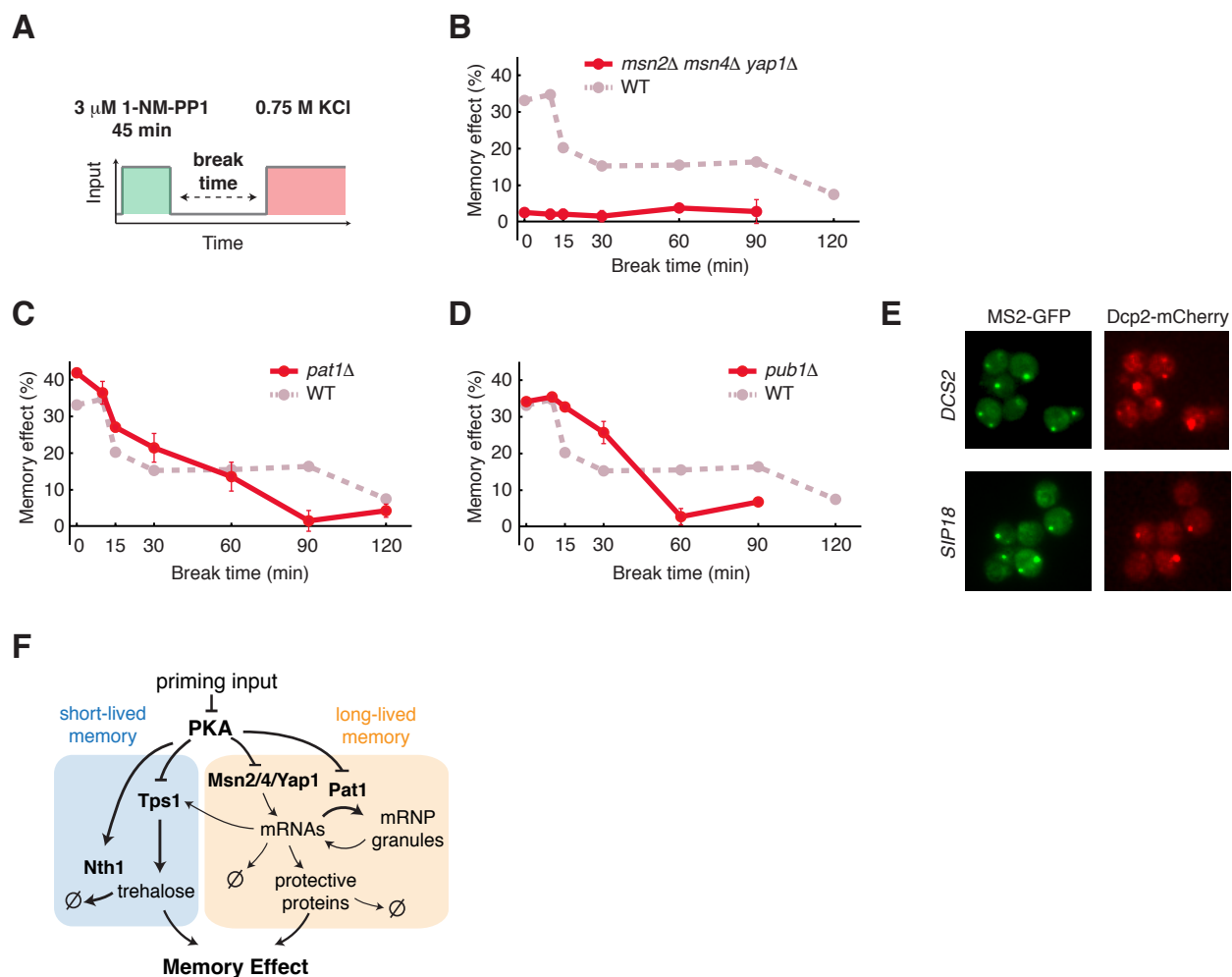
Figure 4. Long-lived memory is mediated by stress-activated TFs and mRNP granules. (A) A schematic of the priming experiment with the high-amplitude prolonged priming input (45 min, 3 μM 1-NM-PP1). Memory dynamics in (B) *msn2Δ msn4Δ yap1Δ*, (C) *pat1Δ*, and (D) *pub1Δ* in response to the high-amplitude prolonged priming input. Data points are averages of at least three independent experiments. Error bars – SEM. Dashed line in dark pink represents the memory dynamics in WT (from Fig. 1F) and is included in the plot for comparison. (E) Co-localization of *DCS2* or *SIP18* mRNAs with PBs (Dcp2-mCherry) in response to 3 μM 1-NM-PP1. Foci formation was observed within 20 min of the input treatment. Representative images were acquired at 170 min. (F) A diagram illustrates the PKA-regulated network that mediates short-lived and long-lived memory.
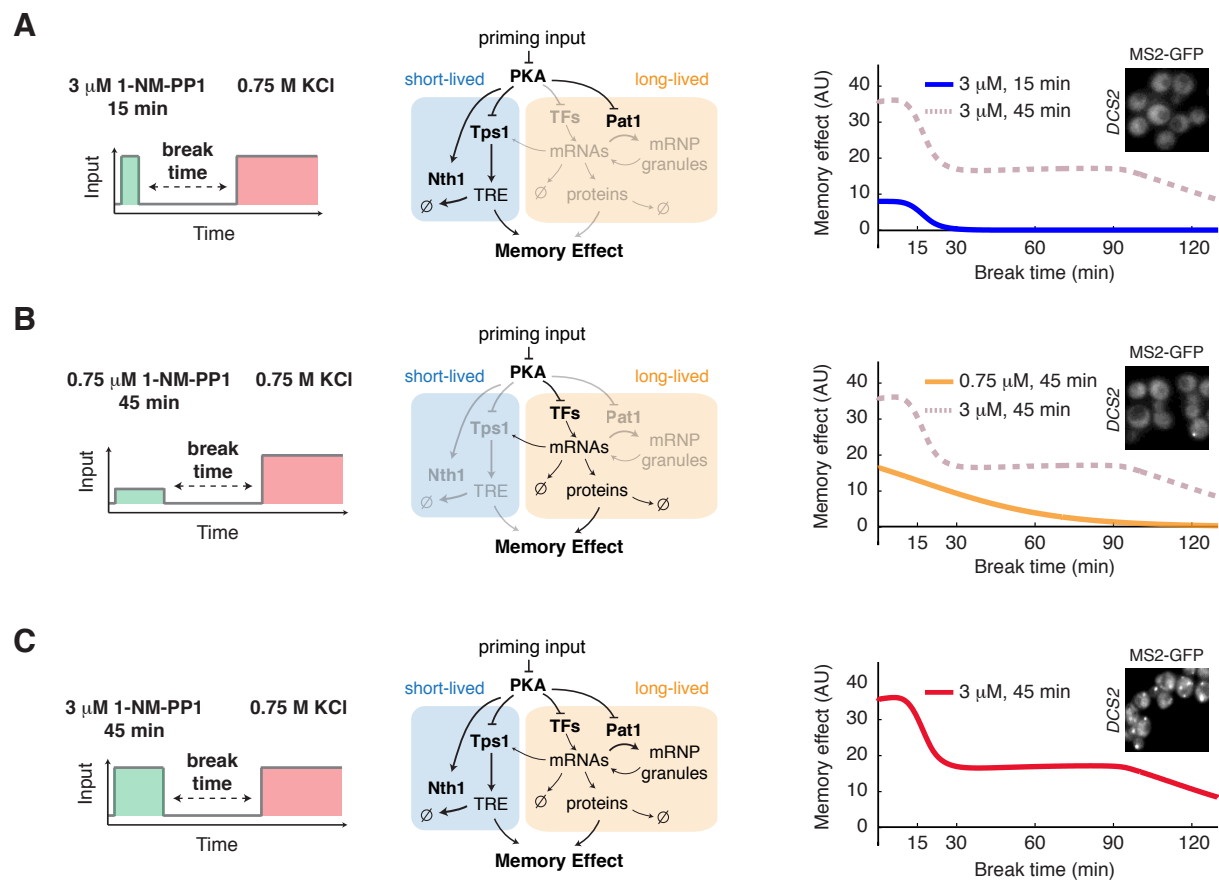
Figure 5. Computational modeling reveals the network-mediated encoding of cellular memory. (A) Model simulation of memory dynamics in response to the high-amplitude transient priming input (15 min, 3 μM 1-NM-PP1). Left panel, the schematic illustrates the treatment procedure. Middle panel, the diagram highlights the part of the network that is activated by the input (black – activated; light gray – not activated). Right panel, the plot shows the simulated dynamics of memory effect. Dashed line in dark pink represents the simulated dynamics in response to the high-amplitude prolonged priming input (45 min, 3 μM 1-NM-PP1) and is included in the plot for comparison. (B) Model simulation of memory dynamics in response to the low-amplitude prolonged priming input (45 min, 0.75 μM 1-NM-PP1). (C) Model simulation of memory dynamics in response to the high-amplitude prolonged priming input (45 min, 3 μM 1-NM-PP1). Insets, the granule formation of DCS2 mRNA in response to indicated inputs. Representative images were acquired at the end of input treatments.
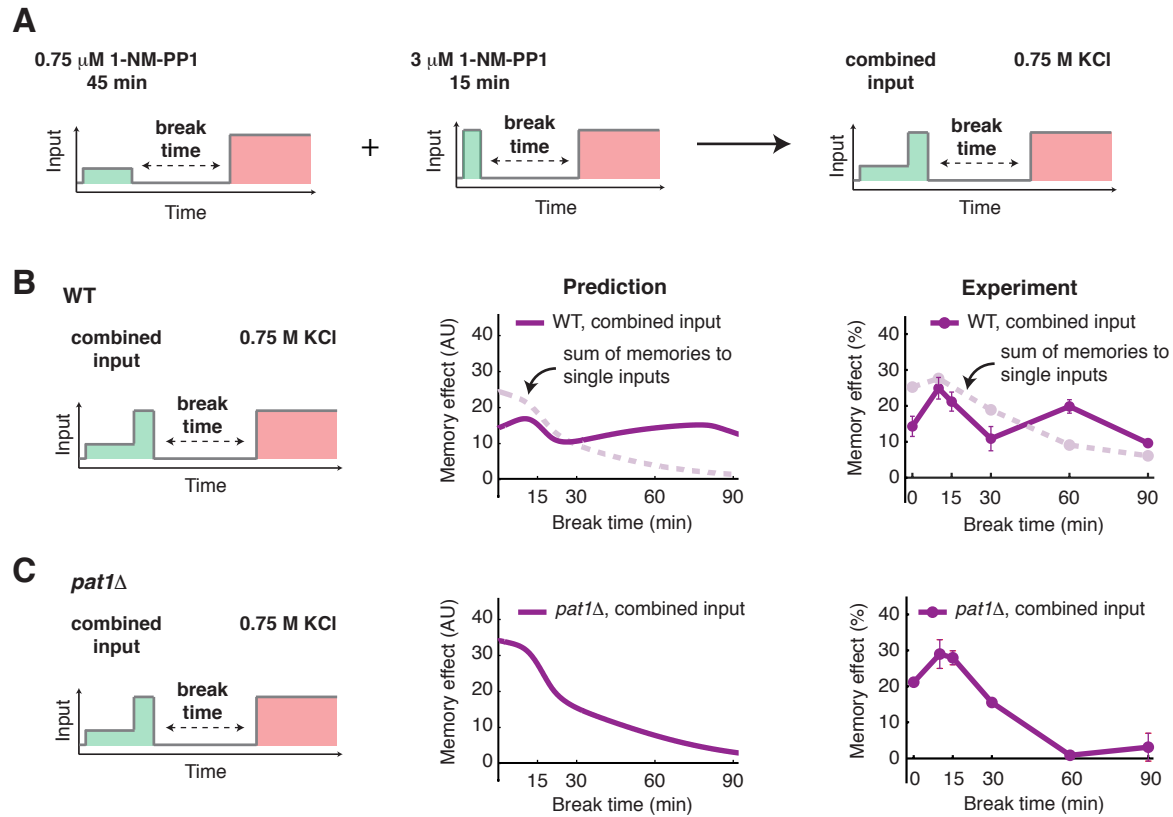
Figure 6. Model prediction and experimental validation. (A) A diagram illustrates the temporally combined input. Two single inputs (45 min, 0.75 μM 1-NM-PP1 and 15 min, 3 μM 1-NM-PP1) were applied sequentially to produce the combined input (45 min, 0.75 μM 1-NM-PP1 followed by 15 min, 3 μM 1-NM-PP1). (B) Model prediction and experimental validation of memory dynamics in WT in response to the combined input. Left panel, the schematic illustrates the treatment procedure. Middle panel, the plot shows the predicted memory dynamics in response to the combined input. Dashed line in light pink represents the sum of memories to two single inputs from Fig. 5A and 5B and is included in the plot for comparison. Right panel, the plot shows the experimentally measured memory dynamics in WT in response to the combined input. Dashed line in light pink represents the sum of memories to two single inputs from Fig. 2B and 2E and is included in the plot for comparison. (C) Model prediction and experimental validation of memory dynamics in *pat1Δ* in response to the combined input.